Electron Beam Welding of Magnesium AZ91D Plates

An investigation into the impact of high cooling rates on microstructure and mechanical properties helps determine optimum welding conditions

BY A. MUNITZ, C. COTLER, H. SHAHAM AND G. KOHN

ABSTRACT. Magnesium AZ91D plates were welded by an electron beam (EB). The integrity of the welded specimens was investigated by X-ray radiography and ultrasonic techniques. Optical and scanning electron microscopy were used to investigate the microstructural changes that occurred during welding. Mechanical properties were determined by standard tension tests. It was found that Mg AZ91D cast alloy can be EB welded with a negligible amount of discontinuities and with a minimal heat-affected zone (HAZ). The rapid melting and subsequent resolidification during welding induces microstructural refinement, which increases both strength and ductility of the alloy. It was also observed the microstructure is finer with less heat flux.

Introduction

Magnesium and magnesium alloys are used in a wide variety of structural and nonstructural applications due to some unique properties such as their low density and high specific strength and elastic modulus (Refs. 1, 2). As such, they are considered as advanced materials for coping with energy conservation and environmental pollution regulations. Thus, magnesium alloys are used for parts in the automotive and aerospace industries where lightweight metals are needed to minimize weight or reduce the internal forces at high accelerations. However, the application of Mg alloys is limited by their poor corrosion resistance and brittleness. Mg-AZ91D, which contains approximately 9 wt-% Al and 1 wt-% Zn, is widely used because of its relatively improved corrosion resistance. Nevertheless, joining of magnesium parts, which may be crucial for these applications, is limited for this alloy (Ref. 3).

There are several welding techniques used for joining Mg alloys. These methods include, among others, arc welding, friction stir welding (FSW) (Ref. 4) and high beam power welding (laser and electron beam). Usually, aluminum content of up to 10 wt-% aids weldability by causing refinement of the grain structure, while a zinc content of more than 1% increases hot shortness, which may cause weld cracking (Ref. 5). Generally, the suitability of a Mg alloy for EB welding is similar as in arc welding. However, there is a substantial difference between gas tungsten arc welding (GTAW) and EB welding. Usually, GTAW involves a high heat input, which causes a broad fusion zone and a very large heat-affected zone (HAZ). In contrast, EB and laser beam welds, due to their concentrated energy, create only narrow fusion zones and have large penetration depths with minimal HAZ (Refs. 6–8). In these processes, high cooling rates are imposed during solidification (Refs. 9–11). These high cooling rates change the solidification path as compared to processes involving slower cooling rates. Since diffusion times and diffusion distances are shorter, different phases may nucleate. A finer grain size is usually associated with faster cooling rates. These changes may reduce the problems involved in arc welding and bring about an improvement of the mechanical properties of the welded parts.

The present work was aimed at optimizing conditions for electron beam welding of Mg AZ91D plates and obtaining a better understanding of the impact of high cooling rates on the microstructure.

KEY WORDS

Electron Beam Welding
EBW
Magnesium Alloys
Mg
Heat-Affected Zone
HAZ
Microstructure
Cooling Rates

Experimental

Magnesium AZ91D ingots of the composition listed in Table 1 were cast and solidified in a permanent mold, then machined into plates of either 2 or 5 mm in thickness. Areas free of solidification pores were chosen for welding using X-ray radiography and ultrasonic pulse-echo techniques. After welding, the plates were minimally machined on both sides. The welded plates were then checked with both techniques. Radiography was performed with a mini-focus X-ray source using a 50-kV voltage and an 8-mA current. A fine-grain film was placed under the plates at a distance of 120 cm from the X-ray tube. Exposure duration was 18 s. Ultrasonic inspection was performed using water immersion. A single 5-MHz transducer was operated in a pulse-echo mode. The transducer was inclined at 22 deg off the normal to the plate surface so that shear waves inclined at 50 deg to the normal were produced inside the plate. The plates were line-scanned, with a resolution of 0.2 mm. Each scanning line was 0.5 mm apart from the other. The sensitivity of the system was calibrated by comparing the ultrasonic images to that of a machined

A. MUNITZ, C. COTLER and H. SHAHAM are with Nuclear Research Center-Negev, Beer Sheva, Israel. G. KOHN is with Rotem Industries, Rotem Industrial Park, Beer Sheva, Israel.

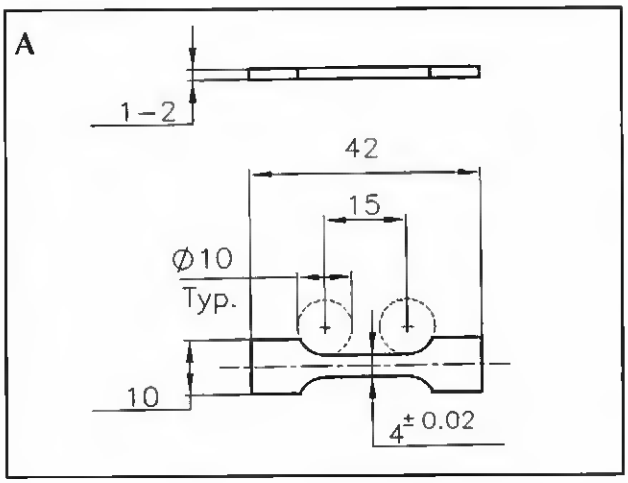

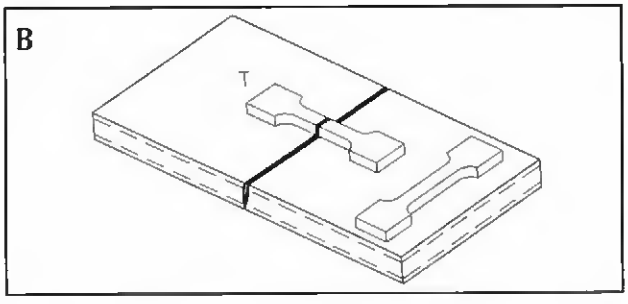

Fig. 1 — A — Schematic drawing of the tension test specimen; B — schematic drawing illustrating two (out of three) tensile specimen types used for analysis.

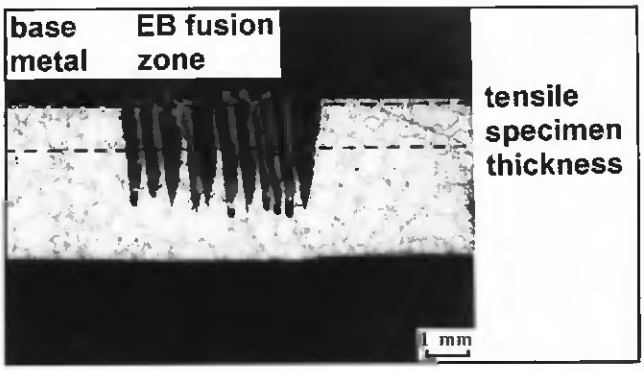

Fig. 2 — Optical micrograph illustrating a cross-sectional view that reveals the EB penetration and the region from which the tensile specimens were manufactured.

cylindrical hole 1 mm in diameter and 0.2 mm deep that could be detected clearly.

In order to find proper electron beam welding parameters, bead-on-plate welds were produced with the following welding parameters: velocity, 10 mm/s; voltage, 6 kV; current, 1.5 or 5.5 mA focused on the surface. The welding conditions were selected to yield full penetration using a minimum power. Welding current of 5.5 mA was used for welding of 5-mm plates, and a welding current of 1.5 mA was used for the 2-mm-thick plates.

To investigate the impact of high cooling rates on the microstructure, Mg plate surfaces were EB melted using the following conditions: velocity, 500 mm/s; voltage, 6 kV; current, 2–7 mA focused on the surface.

For microstructural examination, the welded plates were sectioned and mounted in Bakelite. The specimens were then polished using standard metallographic procedures up to a ¼-micron diamond paste. The specimens were then etched in a solution comprised of 5 mL acetic acid + 5 g picric acid + 10 mL water and 100 mL ethyl alcohol for 20 to 80 s until the microstructure was revealed. The microstructural and compositional analyses were carried out using optical and scanning electron microscopy (SEM). The latter was equipped with an energy dispersive spectroscopy (EDS) attachment. For the EDS analysis, the specimens were etched very lightly, just sufficient to reveal the microstructure yet keep the surface roughness to a minimum. The raw data was corrected with a standard ZAF computer program (Ref. 12).

To avoid the degrading influence of porosity found in the cast ingots on the tensile strength, only defect-free specimens were used. Tensile specimens with 15 mm long and 4 mm wide gauge sections were machined out from the Mg plates, as illustrated in Fig. 1A. This type of specimen preparation allows one to machine from each welding sample three times as many specimens than the number of sub-size tensile ASTM A 370 specimens (60 mm long and 6 mm wide gauge section with total length of 135 mm). Comparison of the results obtained using these different types of specimens shows agreement within 5%. Three types of specimens were machined: 1) base metal in the as-cast condition; 2) specimens containing the EB weld in their center, as illustrated in Fig. 1B and marked with a subscript T; and 3) specimens machined from the EB fusion zone, as illustrated in Fig. 2 and marked with a subscript L. Most specimens were 2 mm thick, except for the specimens manufactured from EB surface-melted areas, whose thicknesses ranged between 1 and 1.4 mm, as described later.

To find the mechanical properties of the EB-melted zone, the surface of the Mg plates was covered with EB passes under the same conditions as in welding to a total width of 6–10 mm. There was an overlap of 20–50% between the passes. A cross section of the melted zone is shown in Fig. 2. The thickness of the tensile specimen was chosen so almost the entire volume of the gauge section was EB melted, as shown by the dashed lines in Fig. 2. To achieve this goal, the upper surface was machined to form a smooth surface, then the plate was machined from the other side to the final thickness according to the actual penetration depth found by the cross-sectional metallography — Fig. 2. Each data point represents an average of at least 2–3 specimens, which were tensioned to fracture in a hydraulic tension machine at a cross-head velocity of 2×10^{-2} mm/s. Fracture surfaces were examined with a scanning electron microscope. To improve resolution by curbing oxidation, the fracture surfaces were gold plated.

For comparison, tensile specimens were also machined from gas tungsten arc and friction stir welded plates (for details on the latter technique, see Ref. 4). Since the weld was wider than 10 mm in both techniques, no problems were encountered in machining the L-type specimens from the weld itself by the same procedure.

Results and Discussion

X-Ray Radiography and Ultrasonic Observation

Ultrasonic examination of the Mg plates prior to welding revealed shrinkage porosity of the order of 20 pm, while X-ray radiography failed to detect these defects (for more details see Ref. 13). It was found the area near the chill, up to 30 mm from the bottom chill, is defect free. All plates were, therefore, welded using specimens prepared from this side

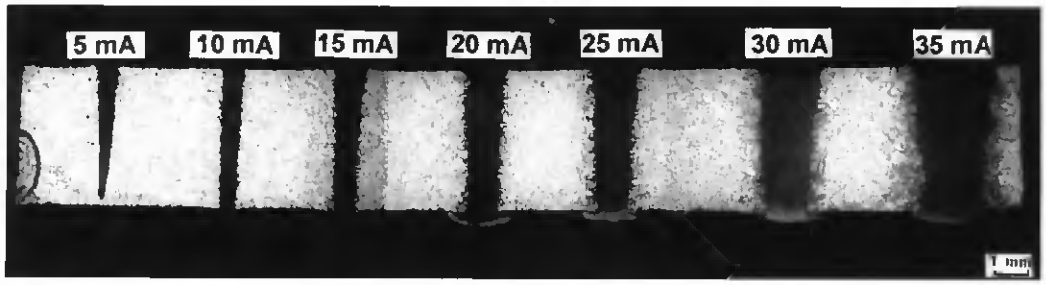

Fig. 3 — Overall macrostructure of bead-on-plate welds on a 5-mm-thick Mg AZ91D plate.

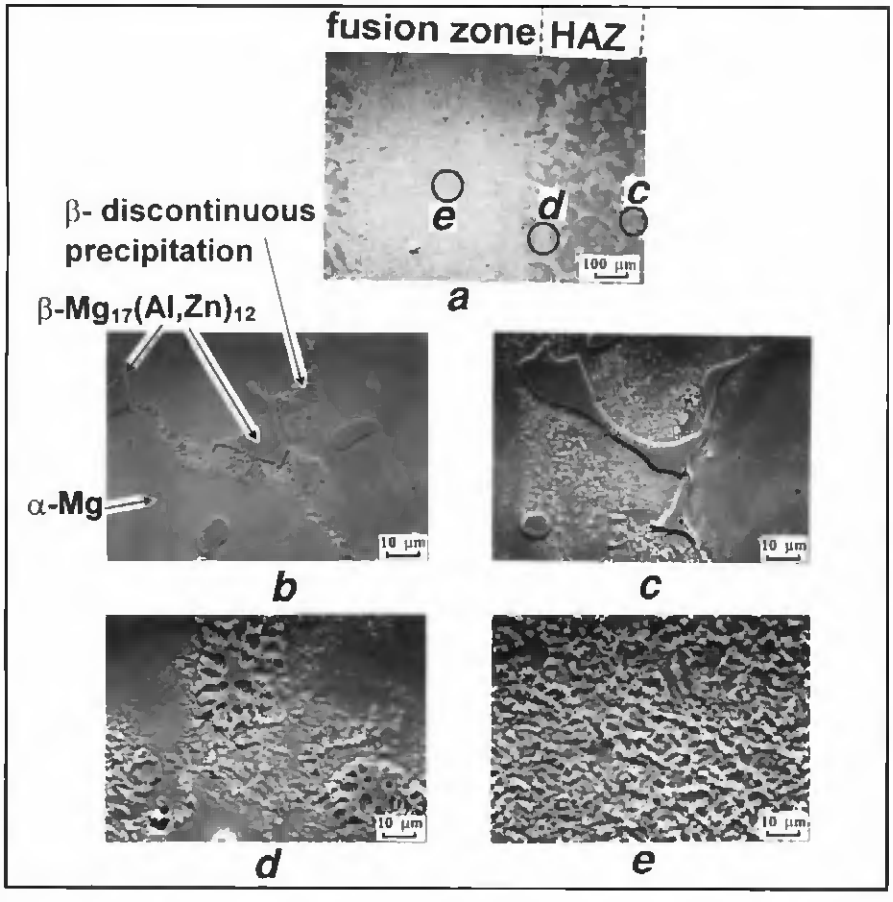

Fig. 4 — Secondary electron images of a top view of an EB weld at a current of 5 mA. A — Top surface overall view; B — as-cast microstructure; C and D — the microstructure of the heat-affected zone far from and near the fusion zone (circles c and d marked in A), respectively; E — fusion zone microstructure (circle e marked in A).

Table 1 — Composition of a Typical AZ91D Ingot Used in the Present Work

Element	Al	Mn	Zn	Si	Cu	Ni	Fe	Be	Mg
Wt-%	8.8	0.24	0.70	0.005	0.0006	0.001	0.0025	0.0007	Bal.

of the ingot. For both welding techniques, when areas free of shrinkage porosity were used, the welded plates were also free of defects such as cracks, voids or shrinkage porosity. Voids present in the base metal almost always affected weld quality.

Microstructural Observation

Bead-on-plate welds with varying welding parameters were performed on a Mg alloy specimen in order to find proper welding parameters. The macrostructure of these welds is shown in Fig. 3. Increasing the current increased both the width of the fusion zones and that of the HAZ — Table 2.

Secondary electron images (SEI) illustrating the microstructure of a typical bead-on-plate weld and its vicinity are shown in Fig. 4. A top overall view is shown in Fig. 4A. Mg AZ91D contains 0.24 and 0.7 wt-% of Mn and Zn, respectively. These additions do not change the major phases of the base metal or of the weld. Therefore, the Mg-Al binary phase diagram (Ref. 14) presented in Fig. 5 will be used to discuss the different phases observed in the microstructure. According to this phase diagram, before welding the base metal consisted of $Al_{12}Mg_{17}$ (ß phase, space group I43m, a-Mn prototype) embedded in between a-Mg dendrites — Fig. 4B. Energy dispersive spectroscopy (EDS) indicates the a-Mg phase contains up to 11.3 and 1.2 at.-% of Al and Zn, respectively, while the average a-Mg contains only 5.0 and 0.5 at.-% of Al and Zn, respectively. This behavior is typical of the coring effect predicated by Schiel's equation (Ref. 15). The ß phase contains about 30 and 2.7 at.-% Al and Zn, respectively. During cooling in the permanent mold, a discontinuous precipitation (Ref. 16) occurred, as marked in Fig. 4B. The ß phase precipitates in the solid state from the supersaturated a-Mg lattice and appears having a "perlite" morphology. Generally this precipitation process begins at grain boundaries and proceeds into the supersaturated a-Mg phase. Upon approaching the HAZ, one could observe that, due to the heating effect, the ß discontinuous precipitates begin to dissolve in the Mg matrix — Fig. 4C. Closer to the fusion zone, the ß phase also begins to dissolve — Fig. 4D. A dendritic microstructure, yet with a refined scale, was observed inside the fusion zone — Fig. 4E.

Secondary electron images (SEI) illustrating the microstructure of an EB weld performed at maximum velocity with a beam current of 3 mA are shown in Fig. 6. In Fig. 6A, a general view of the specimen is shown, demonstrating the penetration of the molten pool into the substrate. The substrate microstructure is shown in more detail in Fig. 4A and was described in detail in the previous section. Figure 6B shows the weld interface between the electron beam fusion zone and the substrate at the maximum penetration depth and protrusion of the unmelted $Al_{12}Mg_{17}$ interdendritic phase into the molten pool. About 10–20 μm from the weld interface, Al-rich bands (as

Table 2 — Width of the Fusion and Heat-Affected Zones as a Function of EB Current for Bead-on-Plate Welds on 5-mm-thick Mg AZ91D Plates

EB Current (mA)	Molten Zone Width (mm)	HAZ Width (mm)
5	0.4	40
10	0.6	52
15	0.9	80
20	1.1	85
25	1.2	110
30	1.6	125
35	2.1	140

Table 3 — Secondary Arm Spacing as a Function of Electron Beam Current

Beam Current (mA)	DAS (μm)	Cooling Rates (K/s)
3	0.7	10^{6}
5	1.25	10^{6}
10	2.25	2×10^{5}
15	3.5	3×10^{5}
20	4.5	10^{5}
25	5.0	7×10^{4}
30	6.0	5×10^{4}
35	7.0	3×10^{4}

Table 4 — Secondary Arm Spacing as a Function of Local Solidification Time for Mg AZ91D (After Bamberger, *et al.*, Ref.19)

DAS (μm)	9.5	9.5	16	17
Local solidification time (s)	1.7	2.6	11	23.5

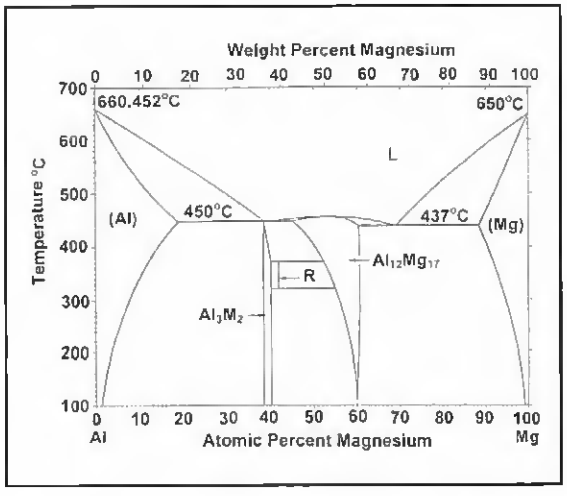

Fig. 5 — The binary Mg-Al phase diagram (Ref. 14).

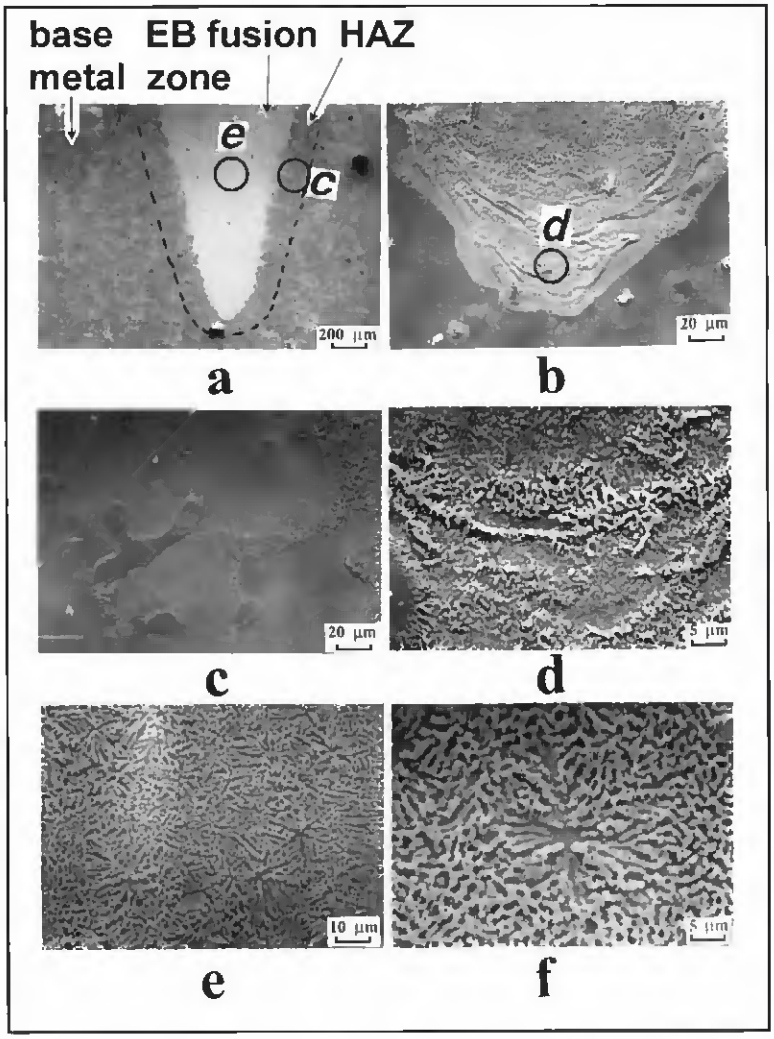

Fig. 6 — Secondary electron images illustrating an electron-beam-melted surface of Mg AZ91D plate. A — Overall weld cross section view; B — microstructure of the weld interface at maximum penetration; C — heat-affected zone near the weld interface (circle c marked in A); D — microstructure at maximum penetration (circle d marked in B); E and F— microstructure at fused area center (circle e marked in A).

compared to the average composition) were observed in the fusion zone — Fig. 6D. The original $Al_{12}Mg_{17}$ phase melted but did not have sufficient time to undergo long-range mass transport due to the short local solidification time. The severe convection existing in the molten pool might cause long-range mass transport creating these compositional bands. However, due to the very short solidification time in the zone near the weld interface, the melt resolidified before long-range diffusion could occur. At a distance of 40–50 μm from the weld interface, a homogeneous melt was created due to the relatively longer solidification time, which allows for convection and diffusion to homogenize the melt. The microstructure of the center of the fusion zone is seen in Fig. 6E to 6F at two different magnifications. Due to the high cooling rates obtained during solidification, microstructural refinement was observed.

Another outcome from the short melting and solidification times of the fusion zone is a very limited dimension of the heat-affected zone (HAZ). As can be seen in Fig. 6C, only a 30- to 50-μm-wide HAZ has been created. Since the melting point of the $Al_{12}Mg_{17}$ phase is about 450°C, as compared to about 600°C for the melting point of the base alloy, the $Al_{12}Mg_{17}$ phase in the HAZ might melt during welding and create molten pockets. These molten pockets may dissolve some of the surrounding Mg matrix. Therefore, upon resolidification of these molten pockets, a broader hollowed $Al_{12}Mg_{17}$ phase is created, as seen on the right-hand side of the photographs in Figs. 5D and 6C.

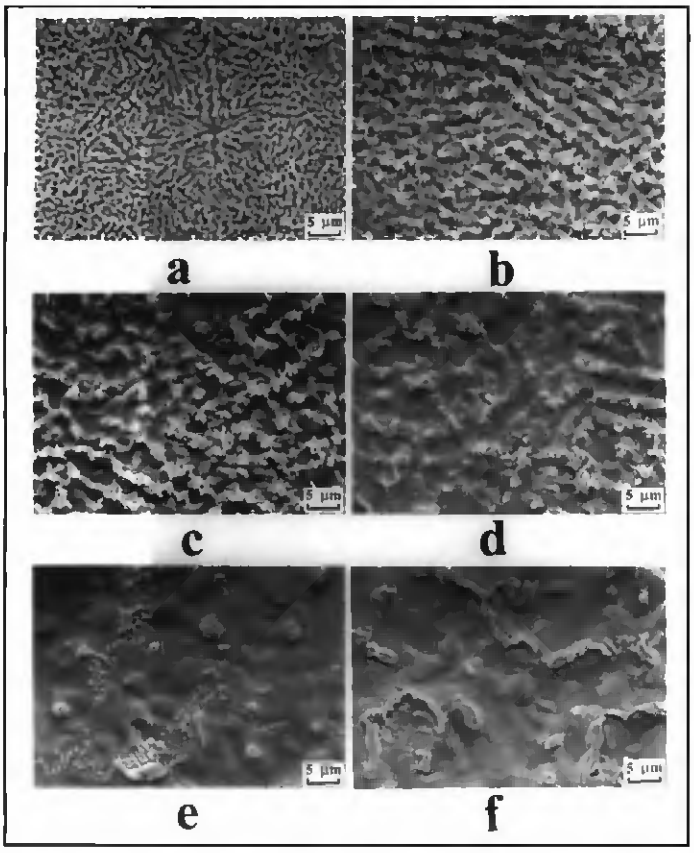

Fig. 7 — Secondary electron images illustrating the microstructure resulting from various welding currents in bead-on-plate experiments. A — 3 mA; B — 5 mA; C — 10 mA; D — 15 mA; E — 20 mA; F — 35 mA.

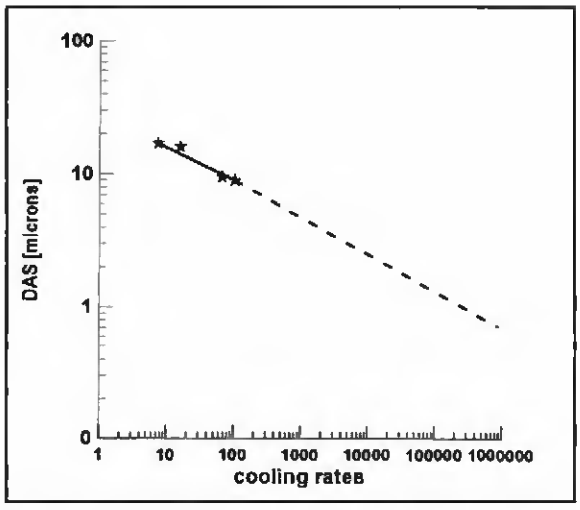

Fig. 8 — DAS as a function of cooling rate after Bamberger, et al. (Ref. 19). The dashed line is an extrapolation of the curve to high cooling rates.

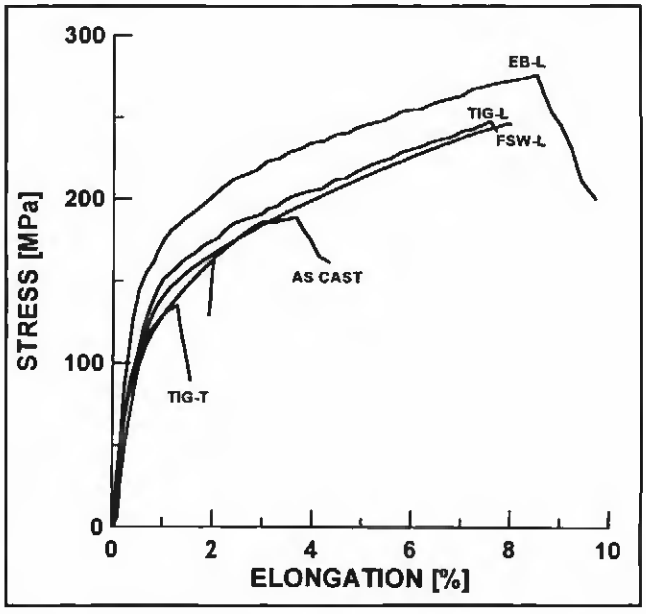

Fig. 9 — Stress/strain curves of various Mg-AZ91D specimens.

Secondary electron images illustrating the microstructure of EB bead-on-plate resolidified zones for various beam currents are shown in Fig. 7. As the beam current increased, larger secondary dendrite arm spacing (DAS) was observed. A summary of the DAS as a function of the beam current is given in Table 3.

In general, the fineness of microstructure during dendritic solidification can be directly related to the local solidification time, t_f, or to the average cooling rate during solidification, e_{avg} (Ref. 17)

$$d = e_{avg}^{-a} = b\, t_f^{n} \qquad (1)$$

$$e_{avg} = \Delta T / t_f \qquad (2)$$

where ΔT is the solidification temperature range, d is the secondary arm spacing and a, b and n are constants. Since the melting temperature of Mg AZ91D is approximately 600°C and the melting temperature of the ternary eutectic (Ref. 18) is about 430°C, we obtain ΔT = 170°C. Bamberger, *et al.* (Ref. 19), has published the data given in Table 4 for the DAS as a function of the local solidification time. Using the data of Table 4 and assuming 170°C as the solidification range, one may plot the DAS as a function of cooling rate, as shown in Fig. 8. If we assume one can extrapolate the curve to the limit of large cooling rates, one may also obtain the cooling rates during EB welding (the cooling rates obtained in this procedure are also given in Table 2). Cooling rates as high as 10^6 K/s could therefore exist during EB welding.

Mechanical Properties

A summary of the mechanical properties for the various EB-melted specimens as compared to those of the as-cast specimens is given in Table 5, and typical stress/strain curves are presented in Fig. 9. For comparison, in Fig. 9 and Table 5, we also included data taken from friction stir and gas tungsten arc welded plates (for more details see Refs. 4 and 13).

As seen from Table 5 and Fig. 9, the yield stress, the ultimate tensile strength and the uniform elongation of specimens prepared from EB welding increased markedly, as compared to those of the as-cast specimens. There is, however, a marked difference between the properties of the GTA-welded and those of the EB-welded specimens. As described in the work of Munitz, *et al.* (Ref. 13), the microstructure of the GTA welded material is similar to the microstructure of the base metal, but with slightly smaller in-

terdendritic arm spacing. Therefore, the stress/strain curve of the GTA-welded material is similar to that of the base metal, with almost the same yield strength. However, because of the finer microstructure in the weld, it continued to work harden with the same slope as that of the base metal, hence the higher σ_{UTS} and larger uniform elongation. On the other hand, the microstructure of the EB surface melted is much finer, hence the additional increase in the yield stress and uniform elongation, as compared to those of the GTA-welded specimens.

Another difference between the GTA-welded and EB-welded specimens is the much smaller HAZ in the latter. This in turn markedly changes the HAZ properties. Degradation of the HAZ mechanical properties in specimens that include the weld in the gauge length (noted with T, Fig. 1) was observed (Table 5 and Fig. 9). All specimens that had the HAZ in their gauge failed, while exhibiting fracture in the HAZ itself. We attribute this fact to the occurrence of continuous ß-phase regions along grain boundaries (Ref. 13). In contrast, the HAZ in EB welding is very small, and the tensile specimens never failed in the HAZ, as illustrated in the top view of tensile specimen microstructure after tension, which is shown in Fig 10.

Table 5 — Summary of Mechanical Properties of As-Cast, Friction-Stir Welded, Gas Tungsten Arc Welded and EB Surface Melted Mg-AZ91D

Sample		Stress Yield (Mpa)	Stress UTS (Mpa)	Elongation Uniform (%)	Elongation Total (%)
Literature (Ref. 3) F temper		97	165	2.5	
As-cast	without pore	136	189	2.6	3.5
	with pores	90	—	0	0
GTAW	T specimen	120	134	0.7	0
	L specimen	152	242	5.8	5.9
Friction stir welding-FSW		136	246	6.7	6.9
EB surface	T specimen	136	189	2.6	3.5
melted	L specimen	152	276	7.3	8.7

Secondary electron images illustrating the fracture morphology of as-cast specimens as compared to those of EB surface-melted specimens are presented in Fig. 11. The fracture surface of the as-cast specimens is mostly intergranular, characteristic of a brittle fracture (Fig. 11A and B). Minor areas in the fracture surface exhibit transgranular dimpled rupture, characteristic of a ductile fracture — Fig. 11B. We attribute these regions to the eutectic regions existing in the as-cast material — Fig. 4B. In contrast, the fracture surface of EB-melted specimens is much finer. At low magnification, the fracture looks brittle — Fig. 11C. However, at larger magnifications, a dimpled microstructure is revealed. This fine microstructure explains the improvement in mechanical properties of the EB-surface-melted specimens.

It should be noted in the fracture surfaces of the EB-melted specimens, some

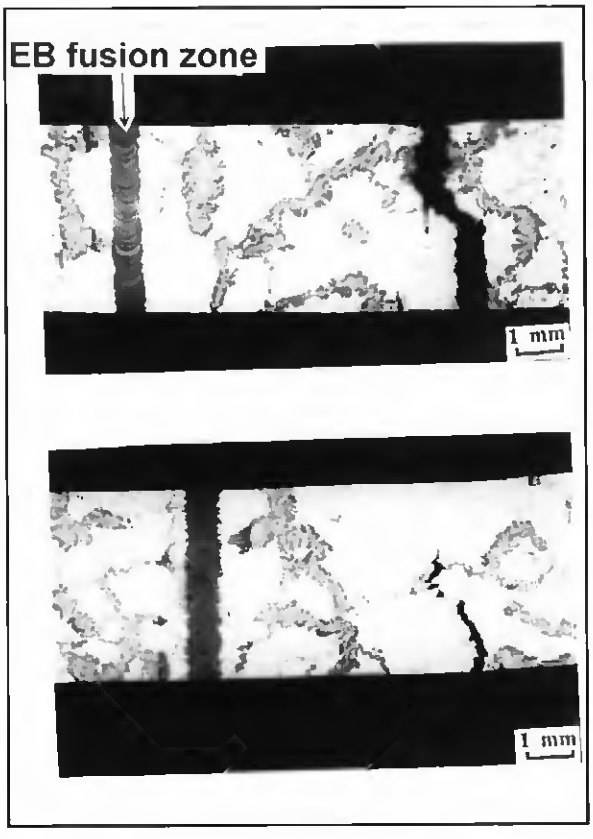

Fig. 10 — Optical micrograph illustrating a top view of a tension specimen showing fracture outside HAZ.

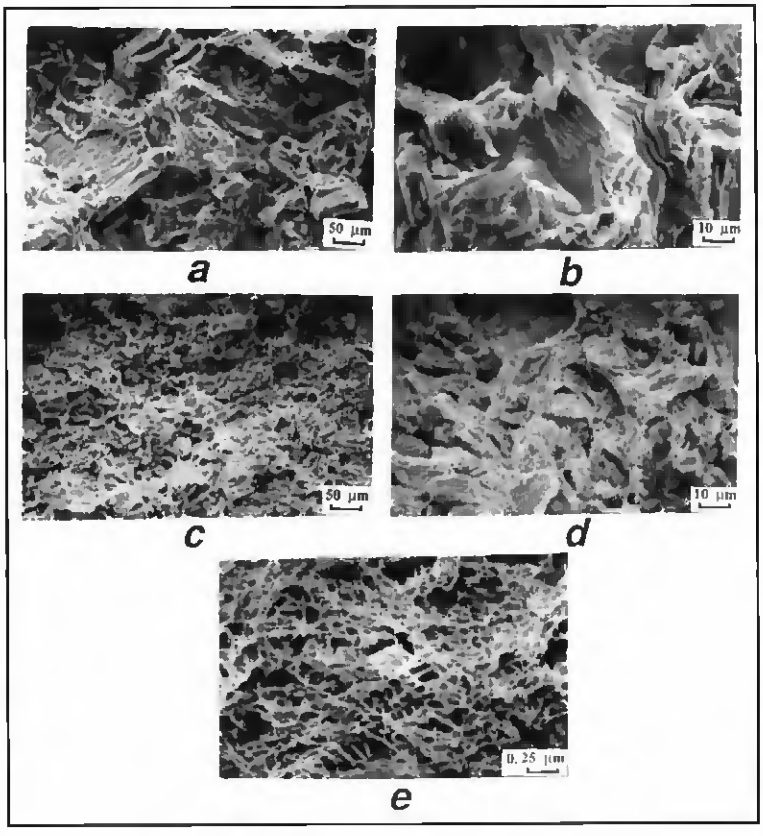

Fig. 11 — Secondary electron images illustrating the fracture microstructure. A and B — The as-cast; C–E — electron-beam-melted surfaces.

residual original as-cast fracture areas occur. Since these areas are relatively brittle, they adversely affect the mechanical properties of the specimens. It was difficult to determine the fraction of volume that has not been melted by the EB. It was, however, reasonable to assume the two EB surface-melted specimens contained different amounts of residual as-cast microstructure. This may explain the differences in the mechanical properties between the two surface-melted specimens.

Summary

Mg AZ91D plates of 2–5 mm thick were successfully electron beam welded under vacuum with no visible defects in either the weld or heat-affected zones. Due to the high cooling rates involved in EB welding, a minimal heat-affected zone with refined microstructure, compared to that of the as-cast material, was obtained. This in turn increased the ultimate tensile strength, as well as the uniform elongation. Cooling rates up to 10^6 K/s were estimated to exist during EB surface melting of Mg AZ91D.

Acknowledgments

The authors wish to thank Z. Burshtein for his critical reading of the mansucript and G. Angel for his technical assistance.

References

1. *Handbook of Ternary Alloy Phase Diagrams,* Eds. P. Villars, A. Prince and H. Okamoto. 1990. p. 3933. ASM International, Materials Park, Ohio.

2. Lee, S., Lee, S. H., and Kim, D. H. 1998. Effect of Y, Sr, and Nd additions on the microstructure and microstructure mechanism of squeeze-cast AZ91-X magnesium alloys. *Met. and Mater. Trans.* A 29A: 1221–1235.

3. *ASM Handbook,* Vol. 2, S. Housh, B. Mikucki and A. Stevenson. 1990. Properties and selection: nonferrous alloys and special-purpose materials, p. 480. ASM International, Materials Park, Ohio,

4. Kohn, G., Antonsson, S., and Munitz, A. 1998. Friction stir welding of magnesium alloys. *Proceeding of the 12th TMS Annual Meeting and Exhibition,* San Diego, Calif., and also presented at the National Welding Conference, Israel.

5. *Metals Handbook,* 9th Edition, Vol. 6, E. F. Nippes, Coordinator. 1983. Welding, brazing, and soldering, p. 427. ASM International, Materials Park, Ohio.

6. Weisheit, A., Galun, R., and Mordike, B. L. 1998. CO_2 laser beam welding of magnesium-based alloys. *Welding Journal* 30: 149-s to 154-s.

7. Draugelates, U., Bouaifi, B., and Brozek, J. 1997. Simulation of laser beam welding of magnesium alloys. *Proc. The First Israeli International Conf. on Magnesium Science and Technology,* Eds. E. Aghion and D. Eliezer, pp. 315–320, Dead Sea, Israel.

8. Draugelates, U., Bouaifi, B., Steinborn, S., Schmid-Fetzer R., and Pisch A. 1997. *Proc. The First Israeli International Conf. on Magnesium Science and Technology,* Eds. E. Aghion and D. Eliezer, pp. 309–314, Dead Sea, Israel.

9. Munitz, A., and Abbaschian, R. 1996. Microstructure of Cu-Co alloys solidified at various supercooling. *Met. and Mater. Trans.* A 27: 4049–4059.

10. Munitz, A., Elder, S., and Abbaschian, R. 1992. Solidification of Undercooled Cu-10 wt-% Co alloys. *Met. Trans.* A 23A: 1817–1827.

11. Munitz, A., and Abbaschian, G. J. 1991. Solid state transformation in Fe-Ni supercooled alloys. *J. of Materials Science* 26: 5195–5202.

12. Reed, S. J. 1977. *Electron Microprobe Analysis.* Cambridge University Press, Cambridge, U.K., pp. 175–197.

13. Munitz, A., Cotler, C., Stern, A., and Kohn, G. Mechanical properties and microstructure of gas tungsten arc welded magnesium AZ91D plates. Submitted for publication in *J. of Materials Sci.*

14. *Binary Alloy Phase Diagrams,* Vol. 1, 1986. Eds. T. B. Massalski, J. L. Murray, L. H. Bennett and H. Baker, pp. 129–130. ASM International, Materials Park, Ohio.

15. Kurz, W., and Fisher, D. J. 1986. *Fundamentals of Solidification,* p. 232. Trans Tech Publications. Switzerland.

16. Porter, D. A., and Easterling, K. E. 1984. *Phase Transformations in Metals and Alloys,* p. 325. Van Nostrand Reinhold, Great Britain.

17. Mehrabian, R. 1982. Rapid solidification. *International Metals Reviews* 27(4): 185–208.

18. *Metals Handbook,* Vol. 2, 9th ed. 1979. Properties and selection: nonferrous alloys and pure metals, pp. 525–535. ASM International, Materials Park, Ohio.

19. Avishai, A., and Bambeger, M., 1999. Relation between cooling rates and microstructures in gravity-die-cast AZ91D disks. *Metallurgical and Materials Transactions* B 30B: 723–729.